How to cite: Angew. Chem. Int. Ed. 2023, e202306091
doi.org/10.1002/anie.202306091

Aluminium Batteries

Redox-Bipolar Polyimide Two-Dimensional Covalent Organic Framework Cathodes for Durable Aluminium Batteries

Yannan Liu[+], Yiyue Lu[+], Arafat Hossain Khan[+], Gang Wang, Yong Wang, Ahiud Morag, Zhiyong Wang, Guangbo Chen, Shengyun Huang, Naisa Chandrasekhar, Davood Sabaghi, Dongqi Li, Panpan Zhang, Dongling Ma, Eike Brunner, Minghao Yu, and Xinliang Feng**

Abstract: Emerging rechargeable aluminium batteries (RABs) offer a sustainable option for next-generation energy storage technologies with low cost and exemplary safety. However, the development of RABs is restricted by the limited availability of high-performance cathode materials. Herein, we report two polyimide two-dimensional covalent organic frameworks (2D-COFs) cathodes with redox-bipolar capability in RAB. The optimal 2D-COF electrode achieves a high specific capacity of 132 $mAh\,g^{-1}$. Notably, the electrode presents long-term cycling stability (with a negligible ≈0.0007 % capacity decay per cycle), outperforming early reported organic RAB cathodes. 2D-COFs integrate n-type imide and p-type triazine active centres into the periodic porous polymer skeleton. With multiple characterizations, we elucidate the unique Faradaic reaction of the 2D-COF electrode, which involves $AlCl^{2+}$ and $AlCl_4^-$ dual-ions as charge carriers. This work paves the avenue toward novel organic cathodes in RABs.

Introduction

The fact that aluminium (Al) represents the most abundant metal element in the earth's crust (8.2 %) brings rechargeable Al batteries (RABs) under the spotlight as a sustainable solution for next-generation energy storage.[1–4] Particularly, the favourable Al stripping/plating chemistry in room-temperature ionic liquids allows the use of non-flammable, capacity-dense (8056 $mAh\,cm^{-3}$, 2981 $mAh\,g^{-1}$) Al metal as RAB anodes, conferring RABs as cheap and safe alternatives to today's lithium-ion batteries.[5–9] One persuasive task for the emerging RABs is seeking proper cathode materials for hosting Al-based ions (e.g., Al^{3+}, $AlCl^{2+}$, $AlCl_2^+$, $AlCl_4^-$, and $Al_2Cl_7^-$).[5,10,11] For example, in the pioneering study by Dai et al., high-rate RABs were assembled using graphitic foam cathodes,[1,12] which stimulated the intensive exploration of graphite-based cathodes.[1,4,13,12] Unfortunately, traditional graphite cathodes are limited by the relatively low specific capacity associated with the large steric hindrance of the $AlCl_4^-$ insertion. Extensive efforts have also been dedicated to employing other inorganic materials to host Al species, ranging from Prussian blue[19] to sulfides,[14] selenides,[3,15] and sulphur.[16] However, their charge-storage processes are severely retarded by the sluggish solid-state diffusion kinetics of Al species due to the strong repulsive interactions with the host materials. Thus, inorganic cathodes usually suffer from unsatisfactory rate performance and cycling performance (>0.1 % capacity decay per cycle) due to the large internal stress and rapid structural collapse during the repeated Al species insertion/extraction.

Unlike inorganic electrode materials, organic redox moieties store charges through a unique coordination mechanism with charge-compensated ions.[5,17] Depending on the charge-compensated ions, organic redox moieties can be categorized into n-type (coordinated with cations), p-type (coordinated with anions), and bipolar-type (coordinated

[*] Dr. Y. Liu,[+] Y. Lu,[+] Dr. G. Wang, Dr. A. Morag, Dr. Z. Wang, Dr. G. Chen, Dr. S. Huang, Dr. N. Chandrasekhar, Dr. D. Sabaghi, D. Li, Dr. P. Zhang, Dr. M. Yu, Prof. X. Feng
Chair of Molecular Functional Materials, Center for Advancing Electronics Dresden (cfaed) and Faculty of Chemistry and Food Chemistry, Technische Universität Dresden
Mommsenstrasse 4, 01069 Dresden (Germany)
E-mail: minghao.yu@tu-dresden.de
xinliang.feng@tu-dresden.de

Dr. Y. Liu,[+] Dr. Z. Wang, Prof. X. Feng
Department of Synthetic Materials and Functional Devices, Max-Planck Institute of Microstructure Physics
06120 Halle (Germany)

Dr. A. Hossain Khan,[+] Prof. E. Brunner
Chair of Bioanalytical Chemistry, Technische Universität Dresden
01062 Dresden (Germany)

Y. Wang, Prof. D. Ma
Énergie Matériauxet Télécommunications, Institut National de la Recherche Scientifque (INRS)
1650 Bd Lionel-Boulet, J3X 1P7 Varennes, QC (Canada)

Dr. P. Zhang
School of Materials Science and Engineering, Huazhong University of Science and Technology
430074 Wuhan (China)

[+] These authors contributed equally to this work.

with cations and anions sequentially).[5,17,18] "Soft" organic redox moieties have aroused intensive interest as RAB cathode materials because they can facilely accommodate complex Al species without inducing large internal stress. Small molecules containing quinone or aromatic amine groups have been demonstrated as desirable high-capacity cathode materials for RABs.[6,8,10,19] Nevertheless, these small molecules generally suffered from fast capacity decay due to the detrimental solubility issue of their redox intermediates.[5,10] To address the durability issue, dynamic covalent chemistries offer a viable way to organize redox-active moieties into polymerized rigid frameworks (such as covalent organic frameworks, COFs) with programmable crystalline order and configurable building blocks. The high rigidity and large polymerization degree of COFs empower redox moieties with strong resistance towards dissolution, which promises COFs with long cycling durability.[7,20–22] On the other hand, the molecularly designable porosity and precisely defined topology of COFs enable the efficient access of redox moieties by ions and thus enhance the efficient utilization of redox moieties.[23,24] In this respect, COF-based cathodes have been demonstrated for relatively mature battery devices, such as Li-ion batteries,[25–28] Na-ion batteries,[29] and Zn-ion batteries.[30,31] Especially, polyimide COFs as n-type or bipolar cathodes hold great promise for high-performance lithium-ion batteries.[32] Nevertheless, constructing advanced RABs with polyimide COF-based cathodes has rarely been explored. It possibly comes from the fact that RABs normally use ionic liquid electrolytes with complex charge carrier species (i.e., $AlCl_2^+$, $AlCl^{2+}$, and Al^{3+}) and high solubility toward organic redox molecules. Thereby, it is essential to rationally design COF structures with configurable building blocks, proper redox active sites, and stable linkages, to enable the reversible hosting of complex Al-based ions and ensure long cycling stability.

Herein, we synthesize two polyimide two-dimensional (2D) COFs by the polycondensation between the monomer of 4,4′,4″-(1,3,5-triazine-2,4,6-triyl)trianiline (TTTA) and two monomers of pyromellitic dianhydride (PMDA) and 1,4,5,8-naphthalenetetracarboxylic dianhydride (NTCDA). The corresponding 2D-COFs are denoted as 2D-PT-COF and 2D-NT-COF, respectively (Figure 1). Both of them depict the redox-bipolar feature by integrating n-type imide and p-type triazine moieties into one framework. Consequently, the 2D-NT-COF electrode achieves a large specific capacity of 132 mAh g^{-1} (referring to the high active-site utilization efficiency of 80.5 %) with a midpoint discharge voltage of ≈1.3 V. In light of the robust imide linkage and the high polymerization degree in the rigid 2D frameworks, the electrode presents ultralong cycling stability (>97 % capacity retention after 4000 cycles, i.e., ≈0.0007 % capacity decay per cycle). Moreover, we unveil the unique redox-bipolar Faradaic reaction of 2D-NT-COF, which includes the reversible reduction of imide moieties with $AlCl_2^+$ as the charge carrier and reversible oxidation of triazine moieties with $AlCl_4^-$ as the charge carrier. We believe that our study provides a platform for an in-depth understanding of the charge carrier and electrochemical behaviour in rechargeable Al batteries.

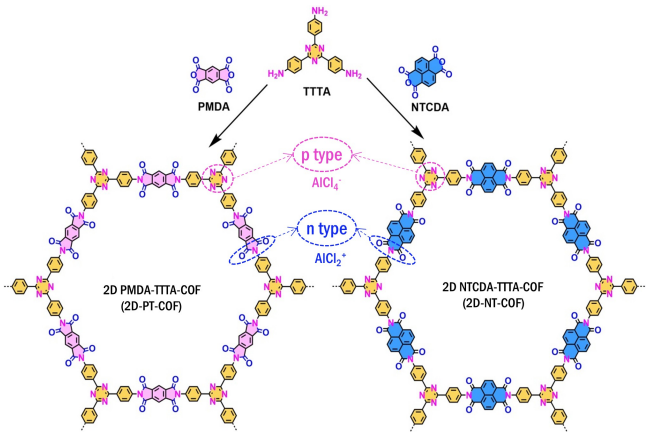

Figure 1. Design and synthetic routes of redox-bipolar 2D-PT-COF and 2D-NT-COF. The combination of n-type imide and p-type triazine moieties enables both 2D-COFs with the sequent anion and cation storage capability.

Results and Discussion

To build the redox-bipolar 2D-COFs, rationally selecting building blocks and linkages is critical for enabling desirable porous topologies for ion storage. Here, imide linkage was utilized to construct polymer frameworks due to the excellent chemical stability and n-type redox feature of its carbonyl groups by reversibly forming negatively charged enolates.[25,33] Meanwhile, TTTA was employed as the second type of building block because the incorporated p-type triazine moieties are expected to reversibly form radical cations by releasing electrons.[34] The synthetic procedures for 2D-PT-COF and 2D-NT-COF are illustrated in Figures 1, S1 and S2 with a detailed discussion in the Supporting Information. Tables S1–S3 summarize the synthetic conditions conducted to obtain the crystalline 2D-COFs. The optimized synthesis of 2D-PT-COF and 2D-NT-COF was achieved by isoquinoline-catalyzed polymerization in a mixture solvent of dimethylimidazolidone (DMI)/mesitylene = 2/1 at 180 °C and a mixture solvent of 1-methyl-2-pyrrolidinone (NMP)/mesitylene = 1/1 at 200 °C, respectively.

^{13}C cross-polarization (CP) magic angle spinning (MAS) nuclear magnetic resonance spectroscopy (NMR) and Fourier transform infrared spectra (FTIR) of both 2D-PT-COF and 2D-NT-COF were carried out to identify their chemical structures. In the solid-state ^{13}C MAS NMR (Figure 2a), both 2D-COFs depict a broad peak at 120–140 ppm referring to the overlapping signal of C–N groups and benzene rings, and two splitted peaks at δ≈160–170 ppm corresponding to the C=O group. Moreover, compared with the corresponding monomers, 2D-NT-COF shows new characteristic FTIR peaks at 1722 cm^{-1} and 1338 cm^{-1}, originating from the C=O symmetric vibration and C–N–C stretching vibration of the six-membered imide rings (Figure 2b).[25] Meanwhile, the characteristic C=O peak at 1769 cm^{-1} of anhydride was not detected for 2D-NT-COF. Similar findings can also be derived by comparing the FTIR

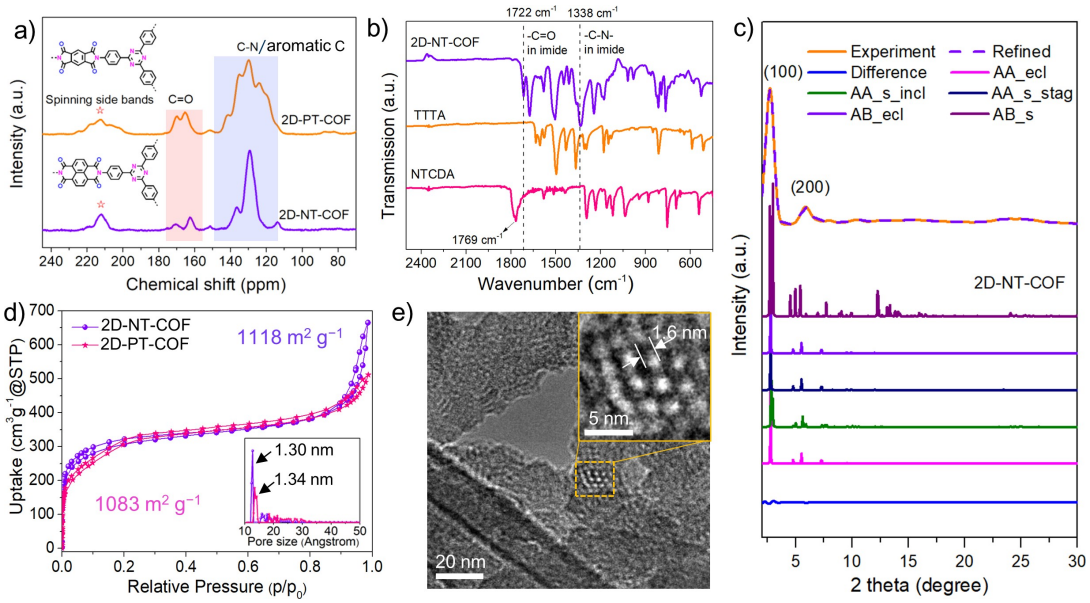

Figure 2. a) Solid-state ^{13}C CP MAS NMR spectra of 2D-PT-COF and 2D-NT-COF. b) FTIR spectra of 2D-NT-COF, 2D-NT-COF30, TTTA, and NTCDA. c) Experimental and simulated PXRD patterns of 2D-NT-COF. d) N_2 adsorption-desorption isotherm curves of 2D-PT-COF and 2D-NT-COF. The insets show the corresponding pore size distribution profiles. e) TEM images of 2D-NT-COF. The high resolution TEM image of 2D-NT-COF is presented in the insets.

spectra of 2D-PT-COF with their corresponding monomers (Figure S3). These results confirm the successful conversion of anhydride monomers into imide linkage in both 2D-COF skeletons.

We assessed the layered crystalline structures of 2D-COFs by powder X-ray diffraction (PXRD). The PXRD patterns of 2D-NT-COF (Figure 2c) and 2D-PT-COF (Figure S4) illustrate an intense (100) peak at 2.7–2.9° and an additional (200) peak at 5.0–6.0°, reflecting their well-ordered crystalline structures. Pawley refinement of 2D-NT-COF ($a=37.14$ Å, $b=37.34$ Å, $c=2.80$ Å, $\alpha=89.8°$, $\beta=89.9°$; $\gamma=120.8°$, Rp = 1.54 %, Rwp = 2.26 %) and 2D-PT-COF ($a=b=36.72$ Å, $c=3.00$ Å, $\alpha=90.0°$, $\beta=90.0°$; $\gamma=120.8°$, Rp = 3.00 %, Rwp = 1.46 %) confirmed their hexagonal crystal structures (see Tables S4 and S5). The simulated structures with AA- and AB-stacking modes (including AA_ecl: eclipsed AA stacking, AA_s_incl: inclined AA stacking, AA_s_stag: staggered AA stacking, AB_s: slipped AB stacking and AB_ecl: eclipsed AB stacking) show similar characteristic PXRD peaks, which raises difficulty in determining the exact stacking mode of these two 2D-COFs.[35] However, the pore size distribution analyses from the N_2 adsorption-desorption measurements (Figure 2d) suggest that both 2D-COFs are preferably organized following the eclipsed AB-stacking mode. In detail, both 2D-COFs present the microporous feature evidenced by the sharply increasing gas uptake in the low-pressure range ($P/P_0=0$–0.99).[36] Nonlocal density-functional theory calculations (the inset of Figure 2d) indicate the dominant pore size of 1.3–1.4 nm, which perfectly matches the simulated pore size (≈1.3 nm) of the eclipsed AB-stacked 2D-NT-COF and 2D-PT-COF, Table S6). Brunauer–Emmett–Teller surface area was estimated to be 1083 $m^2 g^{-1}$ and 1118 $m^2 g^{-1}$ for 2D-PT-COF and 2D-NT-COF, respectively (see Tables S6 and S7).

The sample morphologies were further evaluated by scanning electron microscope (SEM) and transmission electron microscopy (TEM). Evidenced by the SEM images and corresponding energy dispersive X-ray analyses (EDX) (Figures S5–S7), both 2D-PT-COF and 2D-NT-COF appear as large agglomeration consisting of homogeneously distributed carbon (C), nitrogen (N), and oxygen (O) elements. A periodic pattern (ca. ≈1.6 nm) can be observed in the high-resolution TEM (HR-TEM) images of 2D-NT-COF (Figure 2e), corresponding to the d_{100}-spacing of eclipsed AB-stacking 2D-NT-COF. Moreover, 2D-PT-COF showed robust tolerance towards varied liquid environments, such as NMP, concentrated hydrochloric acid (12 M HCl), and the ionic-liquid Al battery electrolyte (denoted IL-1.3) prepared with $AlCl_3$ and 1-ethyl-3-methylimidazolium chloride in a molar ratio of 1.3 (Figure S8), verifying the robustness of the imide linkage.

Next, the electrochemical performance of our 2D-COFs as RAB cathodes was investigated in two-electrode Swagelok cells with Al foil as the anode and IL-1.3 as the electrolyte. Both 2D-COFs were in situ grown on carbon nanotubes (CNTs) with a COF/CNT mass ratio of 7:3 to enhance the charge-transport capability, which would benefit the 2D-COFs to exhibit their intrinsic charge-storage promise.[28,25,27] The obtained hybrid samples are denoted 2D-PT-COF30 and 2D-NT-COF30, respectively. As displayed in the TEM images, tubular core–shell structures with a shell thickness of ca. 10–30 nm were uncovered for 2D-NT-COF30 (Figures S9a and S10) and 2D-PT-COF30 (Figure S11a), which differentiate from pristine CNTs (average diameter of ≈20 nm) with the smooth surface (Figur-

es S12). The uniform coating of 2D-COFs on CNTs driven by the strong π–π interaction is also supported by the corresponding high-angle annular dark-field (HADDF) images (Figures S9b and S11b), elemental mapping images (Figures S9c–e and S11c–e) and additional N elements EDX spectra of 2D-COFs (Figures S13 and S14) comparing with that of pristine CNTs (Figures S15). With such a core–shell structure, highly conductive CNTs offer efficient channel for charge transport within the solid electrode, meanwhile charges are injected/extracted into/from 2D-COFs through the π–π interaction between two phases of CNTs and COFs to trigger the Faradaic redox reaction. Moreover, the similar FTIR spectra of 2D-NT-COF30 (Figure S16) and 2D-PT-COF30 (Figure S3) to these of the pristine 2D-COFs suggests the maintenance of the polyimide structure after the incorporation of CNTs. Additionally, N_2 adsorption-desorption measurements were conducted for 2D-PT-COF30 and 2D-NT-COF30, verifying the well-retained microporosity (Figure S17). 2D-NT-COF30 and 2D-PT-COF30 show relatively lower peak intensity in comparison with that of 2D-NT-COF and 2D-PT-COF, respectively, suggesting the decreased crystallinity degree due to the incorporation of CNTs. All the results indicate the successful preparation of the composites with CNTs and 2D-COFs as core and shell, respectively.

We first compared the cyclic voltammetry (CV) curves of the 2D-NT-COF and 2D-NT-COF30 electrodes at a low scanning rate of 0.3 mV s^{-1} (Figure 3a). For both 2D-NT-COF and 2D-NT-COF30 electrodes, three couples of redox peaks (denoted R1/O1, R2/O2, R3/O3) can be clearly identified, indicating the three-step Faradaic redox reaction associated with the charge-storage process. Kinetics analysis was carried out for the 2D-NT-COF30 electrode (Figure 3b) by collecting its CV curves at various scan rates ranging from 0.3 to 1 mV s^{-1}. The peak current response (i_p) to the applied sweep rate (v) was derived for the two more obvious pairs of broad redox peaks (i.e., R1/O1 and R2/O2), as shown in Figure 3c. According to Equation (1),[25,31] the close-to-1 b-values (0.82, 0.90, 0.97 and 1.02) signify the large contribution of the (pseudo)capacitive process in the charge-storage process of 2D-NT-COF30 electrode (Figure 3c), which benefits from the fast ion diffusion in the well-ordered nanochannels of 2D-NT-COF and efficient electron transport through the CNT core. The high capaci-

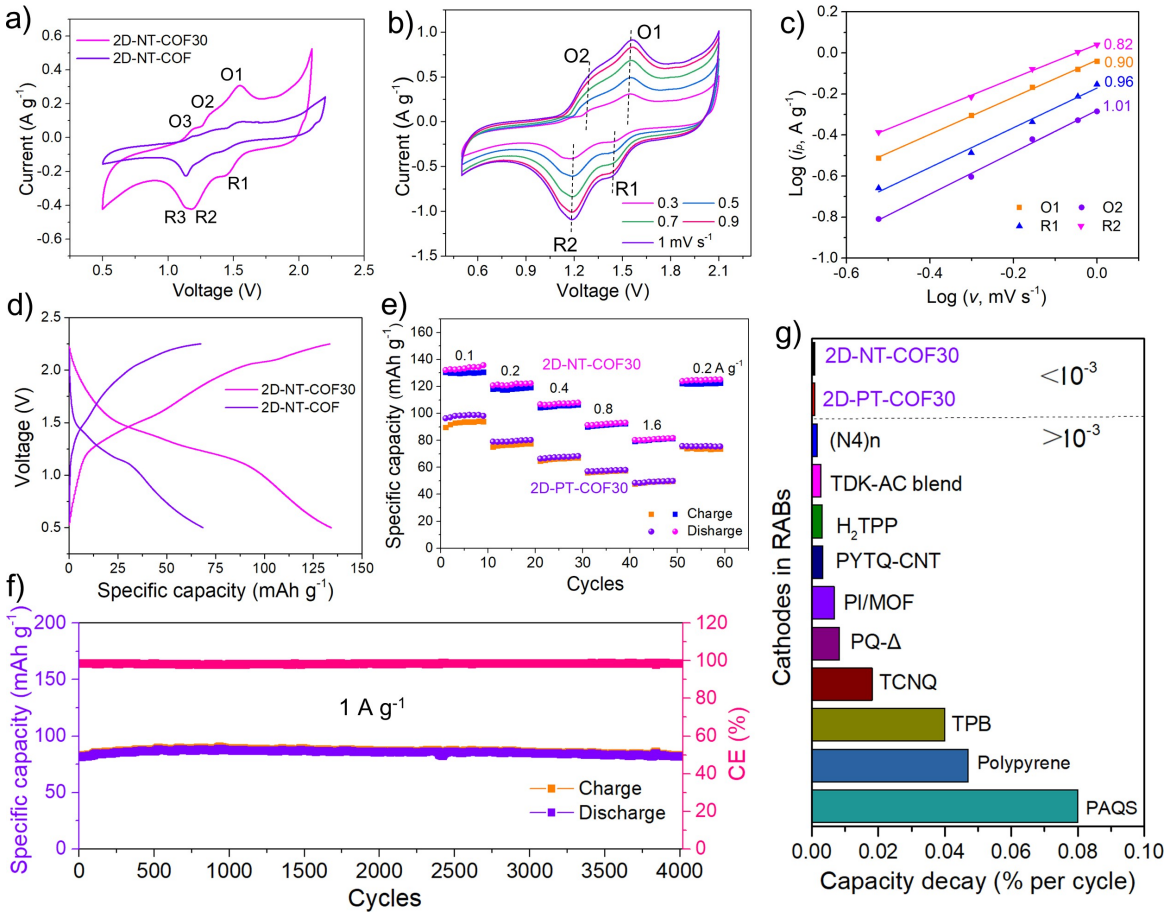

Figure 3. a) CV curves of the 2D-NT-COF and 2D-NT-COF30 electrodes at 0.3 mV s^{-1}. b) CV curves of the 2D-NT-COF30 electrode at various scan rates ranging from 0.3 to 1 mV s^{-1}. c) Log (v) as a function of log (i_p) for the 2D-NT-COF30 electrode. d) GCD curves of the 2D-NT-COF electrode and the 2D-NT-COF30 electrode at 100 mA g^{-1}. e) Rate performance of the 2D-PT-COF30 electrode and the 2D-NT-COF30 electrode. f) Cycling performance of the 2D-NT-COF30 electrode at 1 A g^{-1}. g) Cycling performance (capacity decay rate per cycle) comparison of our electrodes with the reported organic RAB cathodes.[19,20,8,37,6,7,22,1,38–41]

tive contribution was also quantified along with the increasing scanning rate (>70% at 0.5 mV s^{-1} and >80% at 1 mV s^{-1}), as illustrated in Figure S18. Besides, Nyquist plots at the open-circuit voltage indicate the lower internal resistance of 2D-NT-COF30 electrode than that of 2D-NT-COF electrode (Figure S19), confirming the crucial role of CNTs in boosting the charge transport of the 2D-NT-COF30 electrode.

$$i_p = a v^b \quad (1)$$

The galvanostatic charge–discharge (GCD) measurements were further performed for 2D-NT-COF and 2D-NT-COF30 at a variety of current densities. Figure 3d displays the GCD curves of the two electrodes at 100 mA g^{-1}. As expected, 2D-NT-COF30 substantially surpasses the corresponding CNTs-free electrodes in terms of specific capacity. Specifically, the 2D-NT-COF30 electrode presents a high specific capacity of 132 mAh g^{-1} with a midpoint discharge voltage of around 1.3 V. Based on the theoretical specific capacity of 2D-NT-COF (152.7 mAh g^{-1}, Figure S20) and the capacity contribution of CNTs (9.4 mAh g^{-1}, Figures S21 and S22), the 2D-NT-COF30 electrode reached a high redox-site utilization efficiency of 80.5%. By contrast, given the high theoretical specific capacity of 2D-PT-COF (170.9 mAh g^{-1}, Figure S20), the 2D-PT-COF30 electrode only delivered a specific capacity of 91 mAh g^{-1} (Figures S23 and S24), corresponding to a relatively low redox-site utilization efficiency of 53.2%.

The favourable charge-storage performance of the 2D-NT-COF30 electrode is also evidenced by the rate performance (Figure 3e). When the current density increased from 100 mA g^{-1} to 1.6 A g^{-1}, the 2D-NT-COF30 electrode maintained a high specific capacity of 79 mAh g^{-1}, corresponding to the high capacity retention of 59.8%. Meanwhile, the specific capacity of the 2D-PT-COF30 electrode only reached 48 mAh g^{-1} at 1.6 A g^{-1}. By revisiting the chemical structures of the two 2D COFs, the superior charge-storage capability of the 2D-NT-COF30 electrode can be attributed to the larger π-system of the equipped naphthalenetetracarboxylic moieties in 2D-NT-COF than that of pyromellitic moieties in 2D-PT-COF, which helps to efficiently delocalize the injected electrons.[25]

In addition, both the 2D-NT-COF30 electrode (Figure 3f) and 2D-PT-COF30 electrode (Figure S25) present ultralong cycling stability. The initial capacity increase during the long-term cycling test is most likely attributed to an activation process required for electrolyte infiltration. After 4000 charge–discharge cycles at 1 A g^{-1}, the 2D-NT-COF30 electrode presents a low capacity decay of 3.0% (i.e., ≈0.0007% per cycle) with a high average coulombic efficiency (CE, ≈99.9%). Figure S26 uncovers that the GCD curves of the 2D-NT-COF30 electrode at 3900–000 cycles are well overlapped, showing almost identical shapes with the initial charge–discharge profiles. Remarkably, the long-term cycling stability of the 2D-NT-COF30 electrode outperforms that of previously reported organic RAB cathodes (Figure 3g and Table S8).[19,20,8,37,6,7,22,1,38–41] The superb cycling stability of the 2D-NT-COF30 electrode can be explained by the robust imide linkages well reserving the crystalline COF structures. Besides, high rigidity and large polymerization degree of COFs empower redox moieties with strong chemical resistance towards dissolution. This fact can be confirmed by the FTIR spectrum of the cycled 2D-NT-COF30 electrode, in which the characteristic –C=O and –C–N–C– peaks of the imide linkage were clearly detected (Figure S27). Moreover, ^{13}C CP MAS NMR spectra of the pristine and cycled 2D-NT-COF30 electrodes were collected. The identical imide C=O signal at 160–170 ppm was observed for the two electrodes, further suggesting the well-maintained chemical structure (Figure S28). A second reason is that the redox intermediates of 2D-NT-COF have rare solubility in the IL-1.3 electrolyte, which significantly contrasts with small molecules (e.g., NTCDA, Figures S29 and S30). Besides, SEM images of the Al anode before and after the cycling test were collected (Figure S31). No typical tree-like dendrite or filaments were observed on the Al foil. Such a dendrite-free feature also contributes to the high cycling durability of the 2D-NT-COF cathode.

Moreover, we fabricated a new electrode (denoted as 2D-NT-COF30 (811)) by decreasing the super P ratio from 20% to 10%, and the ratio of 2D-NT-COF30: super-P: PVDF is 8:1:1. Figure S32 shows the CV curves of the 2D-NT-COF30 (811) electrode at scan rate of 1 mV s^{-1}. Similar redox peaks in 2D-NT-COF30 (811) can be clearly observed comparing to that of previous 2D-NT-COF30 with the super P ratio of 20%. The 2D-NT-COF30 (811) electrode presents a high specific capacity of 121 mAh g^{-1}at 0.1 A g^{-1} (Figure S33), which is slightly lower than that of the prior 2D-NT-COF30 electrode (132 mAh g^{-1}). Moreover, the 2D-NT-COF30 (811) electrode still presents outstanding cycling stability over 4000 charge–discharge cycles at 1 A g^{-1} (Figure S34). All these results manifest the stable nature of the 2D-NT-COF electrode. Besides, the 2D-NT-COF30 electrode with high loading mass and N/P ratio of ≈3.5 also presents good RAB performance (Figures S35–37), especially excellent cycling stability within 2000 cycles with a high average coulombic efficiency (CE, ≈98.3%).

The attractive performance of 2D-NT-COF30 as the RAB cathode encouraged us to probe into its fundamental charge-storage mechanism. To assign the three couples of redox peaks observed in the CV curve of the 2D-NT-COF30 electrode, we synthesized the imide-containing linear polymer (denoted L-NT-PPD) with NTCDA and p-phenylenediamine (PPD) monomers (Figure S38 and S39). The initial three CV curves of L-NT-PPD and TTTA were then collected in the IL-1.3 electrolyte starting from the open-circuit voltage at rate of 0.3 mV s^{-1}. Two sharp cathodic peaks in the initial CV curve of the L-NT-PPD electrode reveal the n-type feature of imide moieties in L-NT-PPD and their two-step Faradaic redox reaction (Figures S40 and S41).[17] At the same time, a pair of broad redox peaks can be identified from the initial CV curve of the TTTA electrode (Figure S42), indicating its single-step p-type redox feature. Thereby, we can conclude that the 2D-NT-COF30 electrode with integrated imide and triazine moieties well

reserves their respective redox activity and displays the redox-bipolar nature.

We particularly focused on figuring out the charge-compensated species for the 2D-NT-COF30 electrode at different charge states. The EDX (Figure S43) and X-ray photoelectron spectroscopy (XPS) (Figure S44) analyses indicate the presence of both Al and Cl signals with even distribution in both the fully charged and discharged 2D-NT-COF30 electrodes. These results preliminarily suggested the Al–Cl complexes as the charge carrier ions for both n-type imide and p-type triazine moieties. Solid-state ^{27}Al MAS NMR measurements were further performed for the 2D-NT-COF30 electrode at different charge states. Figures 4a and b show the ^{27}Al single-pulse spectra acquired under quantitative conditions. The mixed signals of $AlCl_4^-$ ($\approx$103 ppm) and $Al_2Cl_7^-$ ($\approx$97 ppm) were detected in both the IL-1.3 electrolyte and initial 2D-NT-COF30 electrode at open circuit voltage (electrolyte-soaked electrode, denoted 2D-NT-COF30-OCV) (Figure 4a).[12,1,7] In contrast, only a sharp peak at $\approx$103 ppm was observed for the fully charged 2D-NT-COF30 electrode and TTTA electrode, which manifests that the inserted anionic Al species for the charged 2D-NT-COF30 electrode was mainly $AlCl_4^-$.

In the fully discharged 2D-NT-COF30 electrode, an additional broad signal at ca. 82 ppm was detected, suggesting the appearance of cationic $AlCl_2^+$ (Figure 4b).[42] ^{27}Al spin-spin relaxation (T_2 relaxation, correlated to the dephasing of spin coherence) analysis (Figure 4c) was also carried out for the fully discharged 2D-NT-COF30 electrode based on the spin-echo experiment. Since the immobilization degree of the Al species increases along with the strengthening binding between Al species and the 2D-COF, the shorter T_2 relaxation is normally indicative of the stronger binding of the Al species to 2D-COF. As revealed, $AlCl_2^+$ depicts a much shorter T_2 time (1.2+0.2 ms) than $Al_2Cl_7^-$ (2.3+0.5 ms) and $AlCl_4^-$ (3.1+0.9 ms). Thereby, we infer that $AlCl_2^+$ acted as the charge-compensated ions for the discharged 2D-NT-COF30 electrode, and the strong binding interaction between the 2D-NT-COF30 and $AlCl_2^+$ caused the short T_2 time of $AlCl_2^+$. These results also imply that both $Al_2Cl_7^-$ and $AlCl_4^-$ detected from the discharged samples are most likely due to the adsorbed electrolyte on the 2D-COF electrode. In our lab, we also find that the $AlCl_2^+$ is less stable than $AlCl_4^-$ or $Al_2Cl_7^-$, extensive washing of discharged electrode would destroy or remove $AlCl_2^+$, while certain retention of electrolyte is always happened for repeated experiments after appropriate washing to hold $AlCl_2^+$.

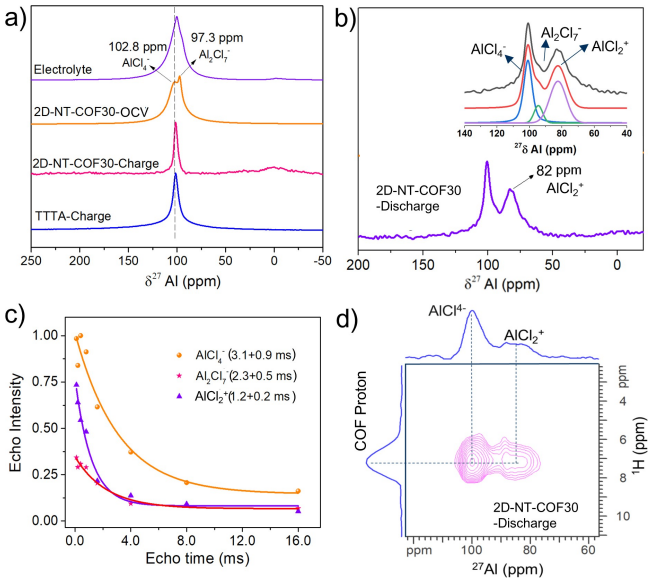

Figure 4. a) Solid-state ^{27}Al MAS NMR spectra of the IL-1.3 electrolyte, 2D-NT-COF30-OCV, the 2D-NT-COF30-Charge electrode (fully charged 2D-NT-COF30), and the TTTA-Charge electrode (fully charged TTTA). b) Solid-state ^{27}Al MAS NMR spectra of the 2D-NT-COF30-Discharge electrode (fully discharged 2D-NT-COF30). Inset shows the deconvolution of the ^{27}Al spectrum. c) Spin echo derived T_2 time of different signals from the 2D-NT-COF30-Discharge electrode. d) 2D ^{27}Al {1H} HETCOR experiment of the 2D-NT-COF30-Discharge electrode with a contact time of 1 ms.

To distinguish the mobile ion species in the electrolyte from the ones of 2D-COF, we executed the dipolar-based back-to-back (BABA)[43] ^{1}H NMR measurement and depth ^{1}H MAS experiment of the discharged 2D-NT-COF30 electrode. The electrolyte signals were suppressed in the ^{1}H BABA experiment compared with the depth ^{1}H MAS experiment due to its high mobility which averages dipolar couplings out (Figure S45). As a result, only the signal of aromatic ^{1}H in the 2D-COF at ca. 7 ppm was detected. Furthermore, the solid-state ^{27}Al {^{1}H} heteronuclear correlation (HETCOR) spectrum based on the through-space interaction between ^{27}Al and ^{1}H was carried out for the discharged 2D-NT-COF30 electrode.[44] As shown in Figure 4d, the aromatic ^{1}H spins of the 2D-COF at 7 ppm observed by the BABA experiment are correlated with the ^{27}Al signals for both $AlCl_4^-$ and $AlCl_2^+$. Compared with $AlCl_4^-$, $AlCl_2^+$ exhibits a relatively broad signal in the cross-polarization HETCOR spectrum. Since the cross-polarization HETCOR experiment relies on the heteronuclear ^{1}H-^{27}Al dipole-dipole coupling, the line broadening of the $AlCl_2^+$ signal could come from the strong immobilization of $AlCl_2^+$ by the 2D-COF framework. This result is in agreement with the directly excited ^{27}Al MAS NMR spectrum, further supporting $AlCl_2^+$ as the charge carrier for the discharged 2D-NT-COF30 electrode. Overall, it is clear that different charge carrier species present in the fully charged ($AlCl_4^-$) and discharged ($AlCl_2^+$) 2D-NT-COF30 electrode.

Furthermore, ^{13}C CP MAS NMR spectra were collected for the 2D-NT-COF30 electrode at different charged and discharged states (Figure 5a). Compared with the pristine and the fully charged 2D-NT-COF30 electrode, the fully discharged 2D-NT-COF30 electrode exhibits apparently weakened imide C=O signal at 160–170 ppm. This finding discloses the reduction of imide C=O in the fully discharged 2D-NT-COF30 electrode, which is accompanied by the binding of $AlCl_2^+$. The apparent line broadening of the imide C=O ^{13}C signal could originate from the heteronuclear ^{13}C-^{27}Al dipole-dipole interaction, as the interaction with quadrupole nuclei (like ^{27}Al) normally induces the line broadening of spin-1/2 nuclei (like ^{13}C) even under MAS

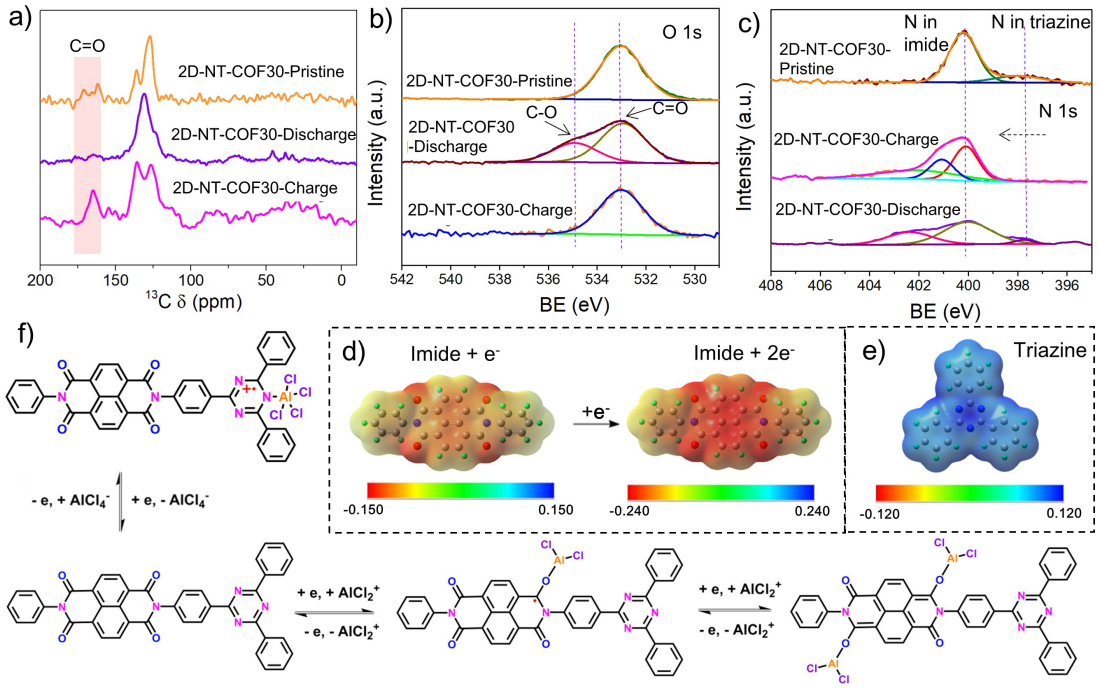

Figure 5. a) ^{13}C cross-polarization MAS NMR, b) O 1s XPS, and c) N 1s XPS spectra of the 2D-NT-COF30 electrode at different charge/discharge states. MESP of d) imide moieties after injected into one or two electrons and e) triazine moieties after extracting one electron. f) The proposed charge-storage mechanism of the 2D-NT-COF30 electrode.

(Figure 5a).[42,45] Additionally, the reduction of the imide C=O bond was manifested by the O 1s XPS spectrum of the fully discharged 2D-NT-COF30 electrode (Figure 5b), in which an additional C–O peak at 534.8 eV associated with the formed enolate species was detected.[46,37] Figure 5c compares the N 1s XPS spectra of the pristine, fully charged, and fully discharged 2D-NT-COF30 electrodes. In the pristine and fully discharged 2D-NT-COF30 electrode, two characteristic peaks at 400.2 and 397.8 eV were identified, corresponding to the imide N and the triazine N, respectively.[47] By contrast, the N 1s peak derived from triazine is upshifted towards a higher binding energy (≈2.7 eV) in the fully charged 2D-NT-COF30 electrode, which supports the oxidation of the triazine by binding with $AlCl_4^-$.[48] Of note, each triazine unit can also receive three electrons by transforming into α-C radicals to storage cations as a n-type redox active site in proper voltage and electrolytes. Meanwhile, the aromatic triazine units are also able to be p-type redox center, and they can be oxidized to form radical cations for anion storage at a relatively high potential, just like our case.

Finally, we calculated the molecular electrostatic potential (MESP) of electron-injected imide moieties of 2D-NT-COF (Figure 5d), as well as the triazine moiety after extracting one electron (Figure 5e).[49] In the electron-injected (one and two electrons) imide moieties, the imide O atoms show the lowest electrostatic potential, indicating their nucleophilic feature to binding cations. Meanwhile, the triazine N atoms show the electrophilic feature with the highest electrostatic potential when one electron is extracted, implying them as the anion binding sites. Based on all-above analyses, we conclude that the charge-storage process of 2D-NT-COF as the RAB cathode material is governed by a unique redox-bipolar reaction (Figure 5f). Specifically, at the fully discharged state, the imide carbonyl groups are reduced to enolates with charge-compensated $AlCl_2^+$ attached to the imide O atoms. At the fully charged state, the triazine moieties are oxidized to form radical cations with $AlCl_4^-$ as charge-compensated species.

Conclusion

In summary, we demonstrated two polyimide 2D-COFs as promising cathode materials for RABs. Both 2D-COFs were designed with the redox-bipolar feature by integrating n-type imide and p-type triazine moieties into one framework. Benefiting from the highly polymerized rigid frameworks, molecularly defined accessible pore channels, precisely engineered topology, as well as dense redox-active sites, 2D-NT-COF30, as the RAB cathode, depicted the outstanding electrochemical performance with a high active-site utilization efficiency of 80.5 %, a large specific capacity of 132 mAh g^{-1} with a decent midpoint discharge voltage of 1.3 V, and ultralong cycling stability over 4000 cycles. We further elucidated the unique redox-bipolar charge-storage mechanism, in which $AlCl_2^+$ (for the reduction of imide moieties) and $AlCl_4^-$ (for the oxidation of triazine moieties) were disclosed to be respective charge carrier species. Our study highlights the feasibility of designing redox-bipolar 2D COFs, which provides insights into constructing advanced

cathodes for emerging battery chemistries with complex charge carrier ions.

Acknowledgements

We thank the financial support from European Union's Horizon 2020 research and innovation programme (GrapheneCore3 881603, LIGHT-CAP 101017821), M-ERA.NET and Sächsisches Staatsministerium für Wissenschaft und Kunst (HYSUCAP 100478697 & Sonderzuweisung zur Unterstützung profilbestimmender Struktureinheiten), the ERC Consolidator Grant (T2DCP, NO. 819698), the DFG for the CRC 1415 (No. 417590517), Polymer-based Batteries (SPP 2248, RACOF-MMIS). We thank Yingying Zhang for the theoretical calculations. The authors also acknowledge the Centre for Information Services and High Performance Computing (ZIH) in Dresden, Germany, for the provided computational resources. The authors acknowledge Dr. Darius Pohl, Dr. Bernd Rellinghaus for the use of TEM facility at Dresden Center for Nanoanalysis (DCN). Open Access funding enabled and organized by Projekt DEAL.

Conflict of Interest

The authors declare no conflict of interest.

Data Availability Statement

The data that support the findings of this study are available from the corresponding author upon reasonable request.

Keywords: Aluminum Batteries · Cathodes · Polyimide · Redox-Bipolar · Two-Dimensional Covalent Organic Frameworks

[1] M.-C. Lin, M. Gong, B. Lu, Y. Wu, D.-Y. Wang, M. Guan, M. Angell, C. Chen, J. Yang, B.-J. Hwang, *Nature* **2015**, *520*, 324.
[2] a) E. Faegh, B. Ng, D. Hayman, W. E. Mustain, *Nat. Energy* **2021**, *6*, 21; b) B. J. Hopkins, Y. Shao-Horn, D. P. Hart, *Science* **2018**, *362*, 658.
[3] Q. Pang, J. Meng, S. Gupta, X. Hong, C. Y. Kwok, J. Zhao, Y. Jin, L. Xu, O. Karahan, Z. Wang, *Nature* **2022**, *608*, 704.
[4] H. Chen, F. Guo, Y. Liu, T. Huang, B. Zheng, N. Ananth, Z. Xu, W. Gao, C. Gao, *Adv. Mater.* **2017**, *29*, 1605958.
[5] Z. Yang, F. Wang, P. Meng, J. Luo, C. Fu, *Energy Storage Mater.* **2022**, *51*, 63.
[6] D. J. Kim, D.-J. Yoo, M. T. Otley, A. Prokofjevs, C. Pezzato, M. Owczarek, S. J. Lee, J. W. Choi, J. F. Stoddart, *Nat. Energy* **2019**, *4*, 51.
[7] G. Wang, E. Dmitrieva, B. Kohn, U. Scheler, Y. Liu, V. Tkachova, L. Yang, Y. Fu, J. Ma, P. Zhang, *Angew. Chem. Int. Ed.* **2022**, *61*, e202116194.
[8] D.-J. Yoo, M. Heeney, F. Glöcklhofer, J. W. Choi, *Nat. Commun.* **2021**, *12*, 2386.
[9] a) J. Tu, W.-L. Song, H. Lei, Z. Yu, L.-L. Chen, M. Wang, S. Jiao, *Chem. Rev.* **2021**, *121*, 4903; b) H. Chen, H. Xu, S. Wang, T. Huang, J. Xi, S. Cai, F. Guo, Z. Xu, W. Gao, C. Gao, *Sci. Adv.* **2017**, *3*, eaao7233.
[10] J. Tu, W. Wang, H. Lei, M. Wang, C. Chang, S. Jiao, *Small* **2022**, *18*, 2201362.
[11] a) K. L. Ng, B. Amrithraj, G. Azimi, *Joule* **2022**, *6*, 134; b) Y. Chen, K. Fan, Y. Gao, C. Wang, *Adv. Mater.* **2022**, *34*, 2200662.
[12] M. Angell, C.-J. Pan, Y. Rong, C. Yuan, M.-C. Lin, B.-J. Hwang, H. Dai, *Proc. Natl. Acad. Sci. USA* **2017**, *114*, 834.
[13] L. Zhang, L. Chen, H. Luo, X. Zhou, Z. Liu, *Adv. Energy Mater.* **2017**, *7*, 1700034.
[14] K. Liang, L. Ju, S. Koul, A. Kushima, Y. Yang, *Adv. Energy Mater.* **2019**, *9*, 1802543.
[15] T. Cai, L. Zhao, H. Hu, T. Li, X. Li, S. Guo, Y. Li, Q. Xue, W. Xing, Z. Yan, *Energy Environ. Sci.* **2018**, *11*, 2341.
[16] a) H. Yang, L. Yin, J. Liang, Z. Sun, Y. Wang, H. Li, K. He, L. Ma, Z. Peng, S. Qiu, *Angew. Chem. Int. Ed.* **2018**, *57*, 1898; b) H. Li, R. Meng, Y. Guo, B. Chen, Y. Jiao, C. Ye, Y. Long, A. Tadich, Q.-H. Yang, M. Jaroniec, *Nat. Commun.* **2021**, *12*, 5714.
[17] P. Poizot, J. Gaubicher, S. Renault, L. Dubois, Y. Liang, Y. Yao, *Chem. Rev.* **2020**, *120*, 6490.
[18] S. Wang, S. Huang, M. Yao, Y. Zhang, Z. Niu, *Angew. Chem. Int. Ed.* **2020**, *59*, 11800.
[19] Y.-T. Kao, S. B. Patil, C.-Y. An, S.-K. Huang, J.-C. Lin, T.-S. Lee, Y.-C. Lee, H.-L. Chou, C.-W. Chen, Y. J. Chang, *ACS Appl. Mater. Interfaces* **2020**, *12*, 25853.
[20] X. Peng, Y. Xie, A. Baktash, J. Tang, T. Lin, X. Huang, Y. Hu, Z. Jia, D. J. Searles, Y. Yamauchi, *Angew. Chem. Int. Ed.* **2022**, *61*, e202203646.
[21] X. Fan, F. Wang, X. Ji, R. Wang, T. Gao, S. Hou, J. Chen, T. Deng, X. Li, L. Chen, *Angew. Chem. Int. Ed.* **2018**, *57*, 7146.
[22] M. Walter, K. V. Kravchyk, C. Böfer, R. Widmer, M. V. Kovalenko, *Adv. Mater.* **2018**, *30*, 1705644.
[23] A. P. Côté, A. I. Benin, N. W. Ockwig, M. O'Keeffe, A. J. Matzger, O. M. Yaghi, *Science* **2005**, *310*, 1166.
[24] M. Yu, R. Dong, X. Feng, *J. Am. Chem. Soc.* **2020**, *142*, 12903.
[25] G. Wang, N. Chandrasekhar, B. P. Biswal, D. Becker, S. Paasch, E. Brunner, M. Addicoat, M. Yu, R. Berger, X. Feng, *Adv. Mater.* **2019**, *31*, 1901478.
[26] H. Gao, Q. Zhu, A. R. Neale, M. Bahri, X. Wang, H. Yang, L. Liu, R. Clowes, N. D. Browning, R. S. Sprick, *Adv. Energy Mater.* **2021**, *11*, 2101880.
[27] H. Gao, A. R. Neale, Q. Zhu, M. Bahri, X. Wang, H. Yang, Y. Xu, R. Clowes, N. D. Browning, M. A. Little, *J. Am. Chem. Soc.* **2022**, *144*, 9434.
[28] S. Xu, G. Wang, B. P. Biswal, M. Addicoat, S. Paasch, W. Sheng, X. Zhuang, E. Brunner, T. Heine, R. Berger, *Angew. Chem. Int. Ed.* **2019**, *58*, 849.
[29] R. Shi, L. Liu, Y. Lu, C. Wang, Y. Li, L. Li, Z. Yan, J. Chen, *Nat. Commun.* **2020**, *11*, 178.
[30] a) W. Wang, V. S. Kale, Z. Cao, Y. Lei, S. Kandambeth, G. Zou, Y. Zhu, E. Abouhamad, O. Shekhah, L. Cavallo, *Adv. Mater.* **2021**, *33*, 2103617; b) S. Zheng, D. Shi, D. Yan, Q. Wang, T. Sun, T. Ma, L. Li, D. He, Z. Tao, J. Chen, *Angew. Chem. Int. Ed.* **2022**, *61*, e202117511.
[31] M. Yu, N. Chandrasekhar, R. K. M. Raghupathy, K. H. Ly, H. Zhang, E. Dmitrieva, C. Liang, X. Lu, T. D. Kühne, H. Mirhosseini, *J. Am. Chem. Soc.* **2020**, *142*, 19570.
[32] a) S. Gu, J. Chen, R. Hao, X. Chen, Z. Wang, I. Hussain, G. Liu, K. Liu, Q. Gan, Z. Li, *Chem. Eng. J.* **2023**, *454*, 139877; b) L. Yao, C. Ma, L. Sun, D. Zhang, Y. Chen, E. Jin, X. Song, Z. Liang, K.-X. Wang, *J. Am. Chem. Soc.* **2022**, *144*, 23534; c) G. Zhao, H. Li, Z. Gao, L. Xu, Z. Mei, S. Cai, T. Liu, X. Yang, H. Guo, X. Sun, *Adv. Funct. Mater.* **2021**, *31*, 2101019.
[33] Q. Fang, Z. Zhuang, S. Gu, R. B. Kaspar, J. Zheng, J. Wang, S. Qiu, Y. Yan, *Nat. Commun.* **2014**, *5*, 4503.

[34] Z. Wang, S. Gu, L. Cao, L. Kong, Z. Wang, N. Qin, M. Li, W. Luo, J. Chen, S. Wu, *ACS Appl. Mater. Interfaces* **2021**, *13*, 514.
[35] Y. Zhang, M. Položij, T. Heine, *Chem. Mater.* **2022**, *34*, 2376.
[36] Y. Liu, S. Fu, D. L. Pastoetter, A. H. Khan, Y. Zhang, A. Dianat, S. Xu, Z. Liao, M. Richter, M. Yu, *Angew. Chem. Int. Ed.* **2022**, *61*, e202209762.
[37] J. Zhou, X. Yu, J. Zhou, B. Lu, *Energy Storage Mater.* **2020**, *31*, 58.
[38] M. Mao, C. Luo, T. P. Pollard, S. Hou, T. Gao, X. Fan, C. Cui, J. Yue, Y. Tong, G. Yang, *Angew. Chem. Int. Ed.* **2019**, *58*, 17820.
[39] N. Lindahl, J. Bitenc, R. Dominko, P. Johansson, *Adv. Funct. Mater.* **2020**, *30*, 2004573.
[40] F. Guo, Z. Huang, M. Wang, W.-L. Song, A. Lv, X. Han, J. Tu, S. Jiao, *Energy Storage Mater.* **2020**, *33*, 250.
[41] J. Bitenc, N. Lindahl, A. Vizintin, M. E. Abdelhamid, R. Dominko, P. Johansson, *Energy Storage Mater.* **2020**, *24*, 379.
[42] L. W. Gordon, A. L. Jadhav, M. Miroshnikov, T. Schoetz, G. John, R. J. Messinger, *J. Phys. Chem. C* **2022**, *126*, 14082.
[43] M. Feike, D. E. Demco, R. Graf, J. Gottwald, S. Hafner, H. W. Spiess, *J. Magn. Reson.* **1996**, *122*, 214.
[44] B.-J. van Rossum, H. Förster, H. de Groot, *J. Magn. Reson.* **1997**, *124*, 516.
[45] J. Bohm, D. Fenzke, H. Pfeifer, *J. Magn. Reson.* **1983**, *55*, 197.
[46] K. Kimura, J. Motomatsu, Y. Tominaga, *J. Phys. Chem. C* **2016**, *120*, 12385.
[47] D. Y. Osadchii, A. I. Olivos-Suarez, A. V. Bavykina, J. Gascon, *Langmuir* **2017**, *33*, 14278.
[48] Y. Gao, C. Dong, F. Zhang, H. Ma, Y. Li, *Polymer* **2022**, *14*, 4804.
[49] a) L. Liu, L. Miao, L. Li, F. Li, Y. Lu, Z. Shang, J. Chen, *J. Phys. Chem. Lett.* **2018**, *9*, 3573; b) P. Zhang, M. Wang, Y. Liu, S. Yang, F. Wang, Y. Li, G. Chen, Z. Li, G. Wang, M. Zhu, *J. Am. Chem. Soc.* **2021**, *143*, 10168.

Manuscript received: May 1, 2023
Accepted manuscript online: May 19, 2023
Version of record online: May 19, 2023

Research Articles

Aluminium Batteries

Y. Liu, Y. Lu, A. Hossain Khan, G. Wang, Y. Wang, A. Morag, Z. Wang, G. Chen, S. Huang, N. Chandrasekhar, D. Sabaghi, D. Li, P. Zhang, D. Ma, E. Brunner, M. Yu,* X. Feng* _____ **e202306091**

Redox-Bipolar Polyimide Two-Dimensional Covalent Organic Framework Cathodes for Durable Aluminium Batteries

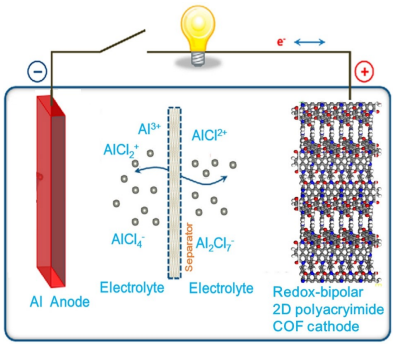

This study provides a proof-of-concept of integrating n-type and p-type active sites into one framework to form redox-bipolar polyimide two-dimensional covalent organic frameworks. The synthesized 2D polymers are demonstrated as attractive cathode materials for Al batteries by enabling both anion and cation storage.